An Arctic Springtime Mixed-Phase Cloudy Boundary Layer Observed during SHEBA

P. ZUIDEMA,* B. BAKER,+ Y. HAN,# J. INTRIERI,@ J. KEY,& P. LAWSON,+ S. MATROSOV,* M. SHUPE,* R. STONE,** AND T. UTTAL@

*Cooperative Institute for Research in Environmental Sciences, University of Colorado, and NOAA/Environmental Technology Laboratory, Boulder, Colorado
+Stratton Park Engineering Company, Boulder, Colorado
#NOAA/National Environmental Satellite, Data, and Information Service, Camp Springs, Maryland
@NOAA/Environmental Technology Laboratory, Boulder, Colorado
&NOAA/National Environmental Satellite, Data, and Information Service, Madison, Wisconsin
**Cooperative Institute for Research in Environmental Sciences, University of Colorado, and NOAA/Climate Monitoring Diagnostics Laboratory, Boulder, Colorado

(Manuscript received 3 November 2003, in final form 11 June 2004)

ABSTRACT

The microphysical characteristics, radiative impact, and life cycle of a long-lived, surface-based mixed-layer, mixed-phase cloud with an average temperature of approximately −20°C are presented and discussed. The cloud was observed during the Surface Heat Budget of the Arctic experiment (SHEBA) from 1 to 10 May 1998. Vertically resolved properties of the liquid and ice phases are retrieved using surface-based remote sensors, utilize the adiabatic assumption for the liquid component, and are aided by and validated with aircraft measurements from 4 and 7 May. The cloud radar ice microphysical retrievals, originally developed for all-ice clouds, compare well with aircraft measurements despite the presence of much greater liquid water contents than ice water contents. The retrieved time-mean liquid cloud optical depth of 10.1 ± 7.8 far surpasses the mean ice cloud optical depth of 0.2, so that the liquid phase is primarily responsible for the cloud's radiative (flux) impact. The ice phase, in turn, regulates the overall cloud optical depth through two mechanisms: sedimentation from a thin upper ice cloud, and a local ice production mechanism with a time scale of a few hours, thought to reflect a preferred freezing of the larger liquid drops. The liquid water paths replenish within half a day or less after their uptake by ice, attesting to strong water vapor fluxes. Deeper boundary layer depths and higher cloud optical depths coincide with large-scale rising motion at 850 hPa, but the synoptic activity is also associated with upper-level ice clouds. Interestingly, the local ice formation mechanism appears to be more active when the large-scale subsidence rate implies increased cloud-top entrainment. Strong cloud-top radiative cooling rates promote cloud longevity when the cloud is optically thick. The radiative impact of the cloud upon the surface is significant: a time-mean positive net cloud forcing of 41 W m^{-2} with a diurnal amplitude of ~20 W m^{-2}. This is primarily because a high surface reflectance (0.86) reduces the solar cooling influence. The net cloud forcing is primarily sensitive to cloud optical depth for the low-optical-depth cloudy columns and to the surface reflectance for the high-optical-depth cloudy columns. Any projected increase in the springtime cloud optical depth at this location (76°N, 165°W) is not expected to significantly alter the surface radiation budget, because clouds were almost always present, and almost 60% of the cloudy columns had optical depths >6.

1. Introduction

Recent decades have witnessed a resurgence of interest in the Arctic climate, initially driven by general circulation model simulations that indicate a strong Arctic response to increasing greenhouse gases (e.g., Houghton et al. 1995). Observations show some support for annual-mean model predictions; these include a rapid warming of the Arctic surface (Chen et al. 2002; Serreze et al. 2000; Stone 1997), decreasing sea ice extent and thickness (Chapman and Walsh 1993; Parkinson et al. 1999), changes in water vapor advection (Groves and Francis 2002), and vegetation changes (Sturm et al. 2001).

An increase in spring and summer cloudiness and decrease in winter cloudiness from 1982 to 1999 has also been noted in satellite data (Wang and Key 2003). Surface observations at Barrow, Alaska, similarly report an increasing spring cloudiness over time (Stone et al. 2002), and increases in springtime cloud optical

Corresponding author address: Dr. Paquita Zuidema, RSMAS, University of Miami, 4600 Rickenbacker Causeway, Miami, FL 33149-1098.
E-mail: pzuidema@rsmas.miami.edu

depth (Dutton et al. 2004). These cloud observations have particular relevance to Arctic climate change as clouds have a strong radiative influence on the Arctic surface energy budget (Curry and Ebert 1992; Intrieri et al. 2002a; Schweiger and Key 1994; Walsh and Chapman 1998), including an influence on the onset date of snowmelt (e.g., Zhang et al. 1996).

Many Arctic clouds are mixed phase,[1] and mixed-phase cloud processes have strong implications for the cloud optical depth. The supercooled liquid contributes prominently to the overall cloud optical depth (Hogan et al. 2003; Sun and Shine 1994) and increases the measured surface infrared flux, especially during the Arctic winter months (Intrieri et al. 2002a). The ice cloud optical depth may be insignificant, but the ice phase indirectly regulates the overall cloud optical depth. The transition to all-ice conditions can be associated with a large drop in cloud optical depth (Curry and Ebert 1992; Sun and Shine 1994).

Most general circulation models do not reproduce even the most basic features of the annual cycle of cloudiness (e.g., Tao et al. 1996). Most likely, this reflects, at least in part, a neglect of mixed-phase microphysical processes (Beesley and Moritz 1999; Vavrus 2004). The liquid phase is common even in subfreezing conditions (Intrieri et al. 2002b; Uttal et al. 2002), despite the ability of ice, when present, to uptake water vapor and liquid quickly; for the −20°C cloud considered here, air saturated with respect to water is 20% supersaturated with respect to ice. More detailed cloud models demonstrate a sensitivity of mixed-phase cloud longevity to modest ice particle and ice freezing nuclei concentrations (Harrington et al. 1999; Jiang et al. 2000; Morrison et al. 2005, hereafter MCSZ; Pinto 1998).

Current deficiencies in model representations of Arctic clouds and their many complex radiation–surface feedbacks support the value of articulating Arctic mixed-phase cloud characteristics, life cycles, and their radiative interactions as completely as possible with observational datasets. The present study examines one multiday Arctic cloud sequence in this light. The focus is on a long-lasting, surface-based, mixed-layer, mixed-phase cloud occurring from 1 to 10 May 1998 at the Surface Heat Budget of the Arctic (SHEBA) site, approximately 3 weeks prior to the snowmelt onset date. This time period overlaps with the first two research aircraft flights of the Arctic Clouds Experiment (ACE; Curry et al. 2000).

A challenge posed to the cloud characterization within this study is the presence of both the liquid and ice phases. The ability to separately characterize the liquid and ice cloud component has remained elusive. Most remote sensors and retrieval methods are designed for only the liquid or ice phase. Methods for simultaneous retrieval using radar–lidar combinations (Hogan et al. 2003; Wang et al. 2004), near-infrared spectra (Daniel et al. 2002), and infrared spectra (Turner et al. 2003) have been proposed, but these are best suited for clouds of low optical depth and do not necessarily provide vertically resolved profiles.

The study presented here uses a conventional approach that lacks these limitations. Retrievals from multiple surface remote sensor measurements [35-GHz cloud radar, depolarization lidar, microwave radiometer (MWR)] are combined with rawinsonde temperature measurements to individually characterize the ice and liquid components. Vertically resolved ice microphysics are retrieved from the cloud radar measurements using a technique developed for all-ice clouds and extended here to mixed-phase conditions. The depolarization lidar establishes the base of the liquid cloud, a temperature inversion identifies the liquid cloud top, and an adiabatic ascent calculation applied to a parcel saturated at cloud base establishes the liquid water content (LWC) profile. Liquid water paths (LWPs) derived from a surface-based microwave radiometer constrain the adiabatically derived LWPs. Comparisons to aircraft data aid and validate the characterization, as does a comparison of modeled to observed radiative fluxes at the surface.

A multisensor adiabatic characterization has been used previously (e.g., Albrecht et al. 1990; Stankov et al. 1995). The approach may be particularly useful for Arctic mixed-phase clouds, as previous observations demonstrate the liquid in nonprecipitating all-liquid or mixed-phase Arctic clouds is often adiabatically distributed (Curry 1986; Curry et al. 1988, 1996; Herman and Curry 1984; Hobbs and Rangno 1998; Jayaweera and Ohtake 1973; Lawson et al. 2001; Pinto et al. 2001; Shupe et al. 2001), a consequence of the often-stable Arctic atmosphere. For the case examined here, the presence of only one liquid layer further eases the determination of the liquid and ice vertical structure. These then provide confidence for a subsequent investigation of the cloud–radiation–surface feedbacks. The influence of the large-scale synoptics on the cloud optical depth is also addressed. The ultimate goal is to aid assessments of future climate change scenarios.

2. Case description and data

a. Surface instrumentation and data description

Table 1 lists the primary surface-based remote sensors used within this study; all are vertically pointing but the sun photometer, which tracks with the sun. The 35-GHz cloud radar retrieval of the ice component is described more fully in section 4a. The cloud radar has a beamwidth of 0.5° and a sensitivity of approximately −46 dBZ at 5 km without attenuation (Moran et al.

[1] A mixed-phase cloud is defined loosely here as liquid and ice coexisting near each other (~<50 m), usually within the same vertical column.

TABLE 1. Surface-based instrumentation.

Instrument	Vertical resolution	Primary application	Instrument reference
35-GHz cloud radar	45 m	Retrieval of ice component	Moran et al. (1998)
23.8- and 31.8-GHz microwave radiometer	Integrated	Liquid water path	Westwater et al. (2001)
0.5235-μm polarized micropulse lidar	30 m	Cloud phase	Alvarez et al. (1998)
Rawinsondes (4 day^{-1})		Pressure, temperature	
Sun photometer (500 and 675 nm)	Integrated	Aerosol optical depth	Stone et al. (1993)

1998). The water cloud bases are established with the depolarization and backscatter unattended lidar (Intrieri et al. 2002b) and rely on both the lidar depolarization ratio and the lidar backscattered intensity. Low lidar depolarization ratios (usually <0.11) indicate sphericity, either from liquid drops or hydrated aerosols. A large gradient in the lidar backscattered intensity further distinguishes the base of a water cloud from aerosol.

LWPs are physically retrieved from the MWR brightness temperatures [Y. Han, unpublished data, see Han and Westwater (1995) for further details]. The physical retrieval uses the dry opacity and cloud liquid absorption models of Rosenkranz (1998) and Liebe et al. (1991), consistent with the recommendations of Westwater et al. (2001). These are all improvements upon the initial SHEBA retrievals. A further strength of the physical retrieval is its use of a liquid cloud temperature estimated from the soundings, the lidar-determined liquid cloud base, and an assumed cloud thickness of 400 m. This reduces the retrieval error to 10 g m^{-2} and represents a valuable improvement on the statistical retrieval error of 25 g m^{-2} (Westwater et al. 2001) for the low LWPs common to the Arctic.[2] The cloud liquid absorption values for temperatures below 0°C are extrapolated from warmer temperature values and therefore less certain. LWPs are retrieved at a 2-min time resolution.

b. Aircraft data description

Table 2 lists the aircraft instrumentation used within this study. We used data from the first and second First International Satellite Cloud Climatology Project (ISCCP) Regional Experiment–ACE (FIRE–ACE) research flights of the National Center for Atmospheric Research (NCAR) C-130 aircraft, occurring on 4 May and 7 May, respectively. LWCs were determined by the mean of the two King hot-wire probes.[3] The King liquid water contents were increased by a factor of 1.2, based upon analysis results by K. Laursen at NCAR of the King probe sensor surface area. The (Forward Scattering Spectrometer Probe) FSSP-100 data establish the drop-size effective radius, and the logarithm of the droplet distribution geometric standard deviation (hereafter referred to as lognormal width).

The FSSP consistently overestimated LWC during the FIRE–ACE project (Lawson et al. 2001), and is more prone to ovestimates in drop sizing than to counting errors. We applied a correction to the FSSP data to achieve consistency with the King probe LWCs (which are thought to be accurate). The FSSP bin sizes were reduced by raising them to a fractional power *a,* where *a* is the ratio between the mean King probe LWC and the FSSP LWC. This effectively reduces the drop sizes, particularly of the largest drops, while preserving the bin concentrations and not allowing the lowest bin to go below 0 μm. Separate values of *a* were calculated for individual time periods.

Statistically meaningful values can be derived from the aircraft liquid water data at a high time resolution. Ice microphysical data are collected at a slower rate by the Cloud Particle Imager (CPI), and approximately 1-min time segments were necessary for constructing a representative size distribution. These correspond to a horizontal distance from the SHEBA site of 4–5 km or less. Complete size distribution spanning from 2 to 2000 μm were estimated from combining the FSSP, CPI, and 260X data. The CPI size distribution is self-scaled on the assumption that the concentration of the larger particles ($\sim$250 μm) can be accurately calculated (Lawson 2003). The 260X probe undercounts particles (Lawson 2003), and in regions where the CPI and 260X size distributions overlapped, the CPI values were chosen. At this point in time, it is difficult to assess the accuracy of the CPI-derived ice concentrations.

After a complete size distribution was estimated, the

[2] The statistical retrieval uses a mean climatological sounding from Barrow, Alaska, rather than the SHEBA soundings, and no information on the liquid cloud altitude or temperature.

TABLE 2. Aircraft instrumentation.

Instrument	Parameter	Range
FSSP-100	Cloud drop and crystal size distribution	2–47-μm particle size
1D OAP-260X*	Drop and crystal size distribution	40–640 μm
Cloud particle imager	Cloud particle phase, shape, and size	5–2000 μm
King hot-wire probe	Liquid water content	0.05–3.0 g m^{-3}

* Optical Array Probe.

[3] One King probe was present on the left side of the airplane, and another on the right side. Their values were typically within 10% of each other.

size distributions were divided into their ice and liquid components. The King probe served as the primary indicator of liquid. The FSSP data were assumed to correspond completely to liquid particles when liquid was present, and the CPI data were partitioned by phase using a roundness criterion. Although the FSSP-100 was probably prone to sizing problems within all-ice conditions, no correction was applied because of a lack of additional information. In liquid-containing regions, the adiabatic shape of the FSSP LWC profile supports the assumption that the FSSP probe senses little ice.

c. Case description

By early May, the SHEBA ice camp had drifted to approximately 76°N, 165°W. Throughout 1–10 May, a low, supercooled liquid cloud persisted within a surface-based mixed layer, and upper ice clouds are apparent within the cloud radar measurements on 4 and 6 May. After 7 May, the low cloud slowly thinned, then dissipated completely at solar noon on 9 May, but developed again later and lasted until mid-May. Two leads, several meters wide, opened near the SHEBA ship around 7 May (Curry et al. 2000). Aspects of the 1–10 May time period are discussed in Curry et al. (2000), Lawson et al. (2001), and Dong et al. (2001), and form the subject of at least two model simulations (Carrió et al. 2005; MCSZ).

The cloud radar reflectivities, lidar-determined water cloud bases, microwave radiometer–derived liquid water paths, and all the temperature soundings from 1 to 10 May are shown in Fig. 1. The lidar, microwave radiometer, and radiosonde measurements indicate the lower cloud contained supercooled liquid (temperature $\sim<-20$°C) while high radar reflectivity values, Doppler velocities, and high radar spectral width[4] values indicate the lower cloud also contained ice [see also Fig. 1 of Intrieri et al. (2002b)]. The upper clouds are likely all ice, based on high values for the radar Doppler velocities, and low values for the radar spectral width.

The radar-reflectivity-determined cloud top usually agreed well with the location of a 2–3-K temperature inversion present during the entire 1–10 May time period (Fig. 2). This temperature inversion persisted during times with low LWPs (6–8 May) and coincided with the liquid cloud top even when the cloud radar data did not clearly distinguish separate low and upper clouds (e.g., Fig. 3). The near-surface temperature averaged approximately −16°C during this time period, with a small warming trend (see also Wylie 2001).

[4] The spectral width is defined as the square root of the variance of sampled Doppler velocities about their mean value. High values can indicate turbulence, but in the Arctic, where turbulence is low, they often indicate a wide distribution of Doppler velocities associated with the presence of two phases. On 4 May, regions determined by the aircraft to contain both phases also corresponded to high values for the radar spectral width.

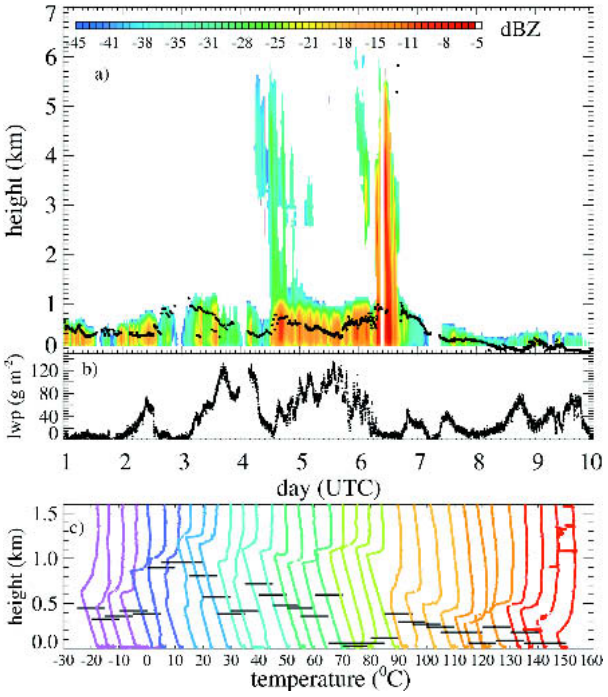

FIG. 1. (a) Radar reflectivities for 1–10 May in dB*Z*, with black dots indicating the lidar-determined water cloud bases, (b) MWR-derived LWP, and (c) all the temperature soundings. Each temperature sounding is displaced by 5°C from the previous sounding, with each day represented by a different color. The lines across the temperature profiles indicate the lidar-determined cloud base.

The 4 May aircraft flight path near the SHEBA site, shown vertically projected upon the cloud radar reflectivities in Fig. 3, coincided with the end of sedimentation from an upper cloud into the lower cloud. We compared liquid water data from one aircraft descent (at 2154 UTC) and ascent (at 2320 UTC) to adiabatic ascent calculations. The aircraft ice microphysical data come from six horizontal overpasses occurring after 2320 UTC and a combination of the overpasses occur-

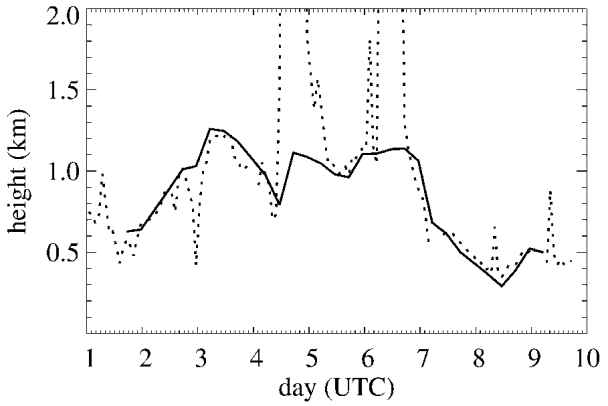

FIG. 2. Radar-determined cloud top (dashed line) and inversion height (solid line) for 1–10 May.

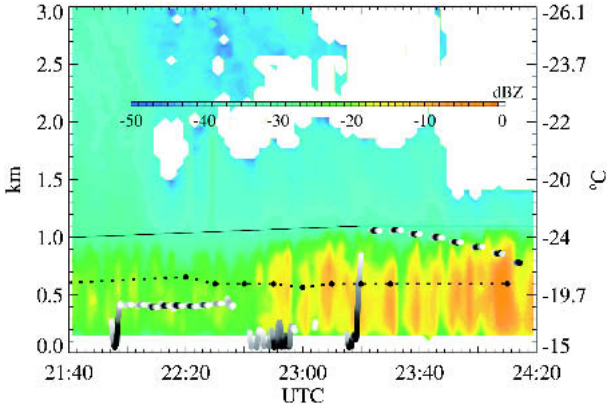

FIG. 3. The 4 May aircraft flight paths occurring within 10 km of the SHEBA site shown vertically projected upon the radar reflectivities, relative to the lidar-determined water cloud base (dotted black line) and the temperature inversion (solid line). Smaller horizontal distances between the aircraft and the SHEBA site are shown in darker shades. Temperatures from the 2300 UTC sounding are indicated on the right axis.

ring between 2200 and 2230 UTC. While the later overpasses occurred within mixed-phase conditions, the earlier overpasses were below the liquid cloud in all-ice conditions.

Mixed-phase conditions were still present on 7 May, but the cloud had thinned, with MWR-derived LWP, falling below their stated error of ± 10 g m^{-2} during the time of the aircraft overflight. We compared liquid water data from three aircraft ascents and descents to the adiabatic parcel calculation.

3. Liquid phase

An LWC profile is determined from the adiabatic ascent of an air parcel just saturated at the lidar-determined cloud base and lifted upward, using the temperature structure interpolated from the nearest-in-time soundings. As the cloud parcel is lifted into colder temperatures, liquid water is condensed until the warmer cloud-top temperature inversion is reached. The vertically integrated LWC is then constrained to match the MWR-derived LWP when the MWR LWP exceeds 15 g m^{-2} (arbitrarily chosen to be 1.5 times the stated error). All the individual temperature soundings show a simple decrease with height until the inversion (Fig. 1c), however, the linear-in-time sonde interpolation can generate a double temperature inversion at some times that foster two (false) relative maxima in the LWC distribution.

Once an LWC profile has been established, the effective radius (r_e) and the volume extinction coefficient (β) are determined. Their derivation uses the mean aircraft-determined cloud droplet number concentration ($\overline{N}$) and a mean aircraft-determined lognormal width $\overline{\sigma_{\log}}$.

a. Liquid water content

Figure 4 shows the adiabatically calculated LWC profiles for the 4 May ascent and descent unconstrained by the MWR-derived LWP, along with the mean King hotwire and FSSP LWCs. The aircraft was close to the SHEBA site at the bottom of the cloud bases, and approximately 20 (descent) or 12 km (ascent) away at the liquid cloud-top height. The lidar-determined cloud base of 600 m coincided very well with the aircraft-sensed base. The adiabatically calculated LWCs, vertically integrated to the aircraft-determined cloud top, are close to the MWR-determined LWPs for both vertical profiles (95% and 103%). A high degree of correspondence between the aircraft and calculated LWCs exists, even over regions separated by 5–20 km. This suggests a horizontally homogeneous liquid layer, with variations in LWP mostly related to variations in the height of the temperature inversion. Horizontal homogeneity in the LWCs is also evident within the aircraft data—during flight segments occurring at constant altitude, the aircraft measurements of LWCs varied by less than 25% of their mean values.

The MWR detected negligible liquid water during the 7 May research flight. A distinct lidar backscattered intensity gradient (though weaker than that of 4 May) allowed the objective placement of the water cloud base. Interestingly, the lidar depolarization ratios were low from cloud base to the surface, which is consistent with either liquid precipitation or aerosols. Since no liquid precipitation was observed by the aircraft, a more likely cause was aerosols. This is consistent with observed ice nuclei concentrations that reached a maximum of 1645 L^{-1} (Rogers et al. 2001), perhaps released from a nearby lead. This situation also demonstrates the utility of applying two separate lidar criteria toward determining the water cloud base.

For all three profiles, the temperature inversion co-

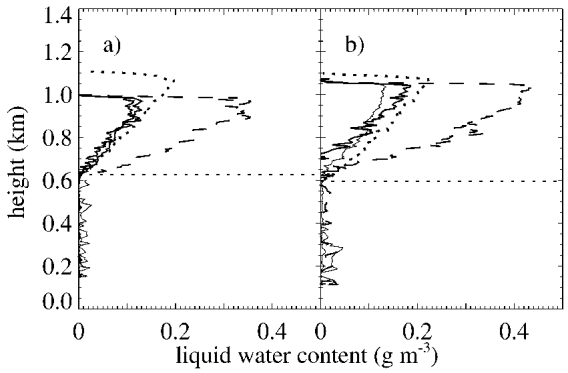

FIG. 4. Aircraft King probe LWC (thin solid line), uncorrected and corrected FSSP-derived LWCs (dashed and thick solid line), and LWCs calculated from an adiabatic ascent and not constrained by the MWR-derived LWP (dotted line) during the 4 May (a) 2153–2155 UTC descent, and (b) 2318–2321 UTC ascent. The lidar-determined cloud base is indicated by a thin dotted horizontal line.

incided to within 20 m of the aircraft-sensed cloud top. The lidar-determined liquid cloud base was often lower than the aircraft-sensed liquid cloud base by 0, 30, and 60 m for the three profiles. This may reflect a spatially varying cloud base, as the lidar cloud base was 30–60 m higher during the previous hour. Two of the three profiles are shown in Fig. 5, and indicate the aircraft LWCs are close to their adiabatic maximum values. The lidar–radiosonde adiabatic combination was therefore able to correctly detect and distribute liquid in a low-LWP situation where the MWR LWP retrieval was quite uncertain.

b. Determination of N and $\sigma_{\log}$

The mean values of N and $\sigma_{\log}$ were determined from the corrected FSSP drop-size distributions of the five aircraft vertical profiles. Only FSSP number concentration values exceeding 50 cm^{-3} were used, reflecting a screening for ice particles (results were not sensitive to the threshold value). We find a time-mean N of 222 cm^{-3}, with a standard deviation, using the means of each individual time period, of 14 cm^{-3}. Furthermore, N varies little with height during any of the five vertical profiles. Observed number concentrations were high relative to the overall FIRE–ACE time period, coinciding with a polluted layer overlying the cloud (Yum and Hudson 2001), or reflecting aerosol input into the atmosphere from the open leads near the ship.

The lognormal width of the distribution can be derived from the observable parameters as

$$\sigma_{\log} = \left[\frac{-1}{3}\ln\left(\frac{6\mathrm{LWC}}{\pi\rho_w N D_e^3}\right)\right]^{0.5} \quad (1)$$

(Miles et al. 2000) where ρ_w is the density of water and D_e is the effective particle diameter. All values come from the corrected FSSP drop-size distributions. A mean value of $\overline{\sigma_{\log}} = 0.242 \pm 0.015$ was determined, and a slight spectral narrowing with height is evident within all five vertical profiles.[5]

c. Liquid effective radius and volume extinction coefficient

The effective radius r_e is modeled following the method and notation of Frisch et al. (1995) as

$$r_e = r_o \exp\left(\frac{5\sigma_{\log}^2}{2}\right), \quad (2)$$

where r_o is the modal radius in microns and a lognormal droplet size distribution is assumed. The effective radius is calculated every 10 min in terms of the observables LWC, $\overline{N}$, and $\overline{\sigma_{\log}}$ as

$$r_e = \left(\frac{3\mathrm{LWC}}{4\pi\rho_w\overline{N}}\right)^{1/3} \exp(\overline{\sigma_{\log}}^2)(1000), \quad (3)$$

where LWC and ρ_w are in g m^{-3}, $\overline{N}$ in cm^{-3}, and r_e in μm. The volume extinction coefficient β is similarly calculated assuming the geometric optics limit (extinction equal to twice the integrated droplet cross-sectional area) as

$$\beta = 2\pi\overline{N}r_e^2 \exp(-3\overline{\sigma_{\log}}^2)(0.001), \quad (4)$$

with β in km^{-1}.

A sample comparison between the adiabatically derived and aircraft r_e and β for the 4 May descent is shown in Fig. 6. Figure 7 shows a comparison for the liquid optical depths (τ) derived from the aircraft data and from the adiabatic retrieval (with $\overline{N} = 222$ cm^{-3} and $\overline{\sigma_{\log}} = 0.242$), for all five aircraft descents/ascents.

[5] This is consistent with traditional theory of condensational droplet growth for an adiabatic parcel experiencing no mixing or gravitational collection and was also observed during the Atlantic Stratocumulus Transition Experiment (ASTEX; Gerber 1996), but is counter to most other observations (Miles et al. 2000).

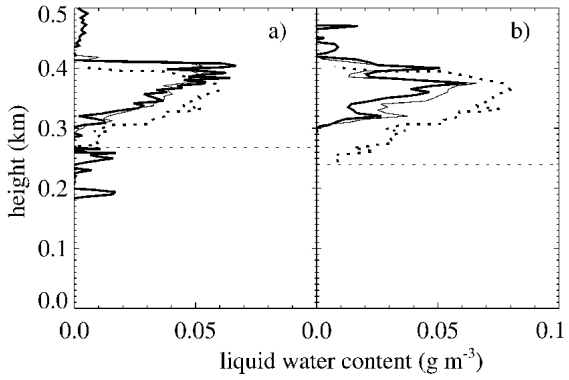

FIG. 5. Corrected FSSP and King probe LWCs (thin and thick solid lines) and the adiabatic LWC (dotted line) during the 7 May (a) 2216–2219 UTC descent, and (b) 2307–2330 UTC overflights binned by altitude. The lidar-determined cloud base is indicated by a horizontal dotted line.

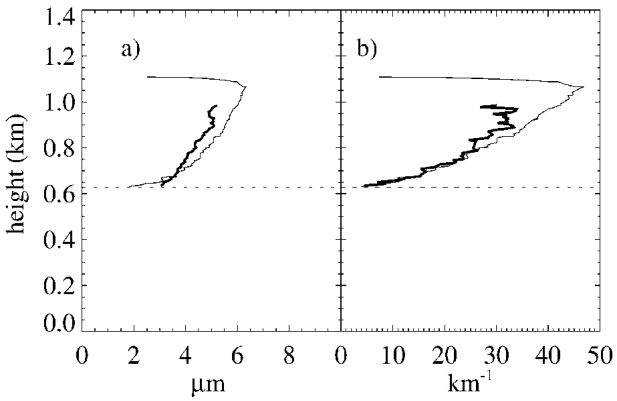

FIG. 6. Comparisons during the 4 May 2153–2155 UTC descent between the aircraft (thick line) and adiabatically derived (thin line; $\overline{N} = 222$ and $\overline{\sigma_{\log}} = 0.242$) (a) effective particle radius and (b) volume extinction coefficient.

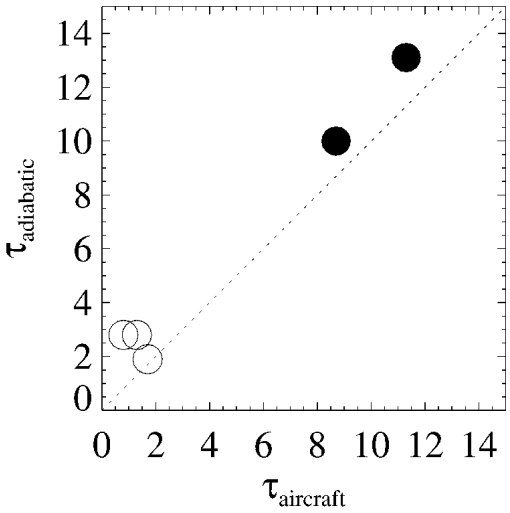

FIG. 7. Cloud optical depth determined through a vertical integration of Eq. (4) vs aircraft-corrected FSSP drop-size distributions for 4 May (filled circles) and 7 May (open circles).

For the 4 May time periods when the MWR-derived LWP constrained the adiabatic calculation, the agreement is to within 10%. For the 7 May time periods, the MWR-derived LWP was below the noise threshold and was not used, and the agreement is worse, but this reflects a different cloud-base placement by the lidar and the aircraft (Fig. 5).

d. The 1–10 May liquid phase time series

Liquid β and r_e, derived from the observed LWC, $\overline{N}$, and $\overline{\sigma_{\log}}$ using Eqs. (4) and (5), are shown for the 1–10 May time period in Fig. 8, along with the optical depth and layer-averaged effective radius. The mean cloud optical depth is 10.1 ± 7.8, corresponding to a mean LWP of 37 g m^{-2}. The layer-mean effective radius is 4.4 ± 1.1 μm, the time-mean cloud top effective radius is 5.4 ± 1.5 μm (this value is most consistent with the time-mean LWP and optical depth), and the LWC-weighted effective radius is 4.8 ± 1.3 μm. These effective radii values are approximately one-half of those reported in Dong et al. (2001) for coincident time periods, a consequence of the correction made to the FSSP data in this study, an improved microwave LWP retrieval, and the use of the aircraft-determined $\overline{N}$ within the effective radius calculation. Physically, the low values reflect cloud droplet concentrations that are anomalously high for the Arctic; possible aerosol sources exist above the boundary layer and from nearby open leads. Cloud optical depth maxima of approximately 30 are apparent on 3 and 5 May, times when no upper cloud was detected and the boundary layer was deeper.

4. Ice phase

In contrast to the liquid phase, the retrieval of the ice component depends only on one instrument, the 35-GHz cloud radar. Comparisons between radar and aircraft-determined mean microphysical values are more uncertain for ice than for liquid, however. The cloud radar retrievals are plagued by insensitivity to the smaller particles and to the particle habit (for cloud radars lacking polarization) and rely on individual particle density–size and mass–area–size relationship assumptions. Particle habit also introduces uncertainty into the calculations based on the aircraft data. Additionally, for the aircraft data, the complete size distributions require a compilation of data from three or four instruments sensing different size ranges.

We estimate an effective ice particle diameter $D_{e,i}$ from the ratio of the total ice water content (IWC) to the total projected area (Matrosov et al. 2003; Mitchell 2002), or,

$$D_{e,i} = 1.5 \frac{\text{IWC}}{\rho_i A_p}, \tag{5}$$

where ρ_i is the solid ice density of 0.917 g m^{-2}, and A_p is the total projected particle area. This definition represents an effective photon path for a size distribution, or a representative distance that a photon travels without reflecting or refracting within a representative particle (Mitchell 2002). For spherical particles, $D_{e,i}$ reduces to the similar liquid cloud effective diameter standard. This definition of $D_{e,i}$ preserves those quan-

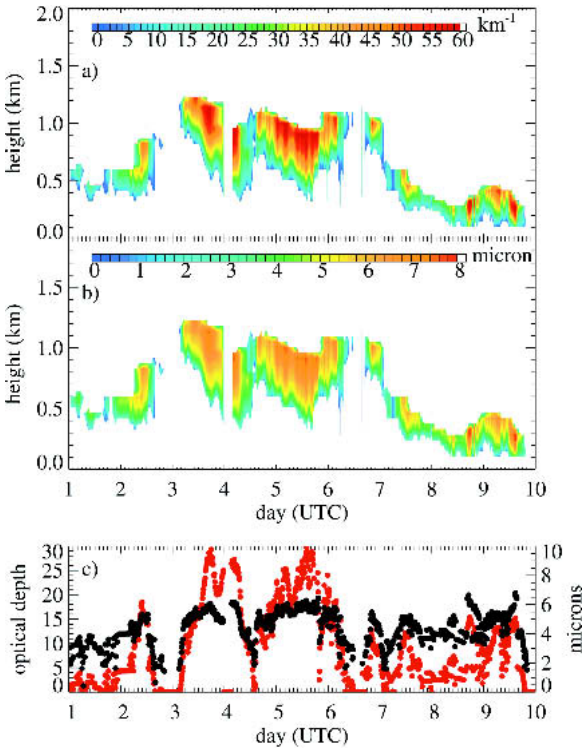

FIG. 8. The liquid (a) volume extinction coefficient, (b) effective radius, and (c) optical depth (red) and layer-mean effective radius (black) calculated from the observed LWC, $\overline{N}$, and $\overline{\sigma_{\log}}$.

tities important to the radiative transfer, namely, the total mass and the total cross-sectional area (e.g., Fu 1996).

In practice, we first estimate IWC and β_i, assume an extinction efficiency of 2, and calculate $D_{e,i}$ from

$$D_{e,i} = 3\frac{\text{IWC}}{\rho_i \beta_i}. \quad (6)$$

By first performing an independent estimate of the volume extinction coefficient and then deriving the effective particle diameter estimate, $D_{e,i}$ cannot impact the optical depth estimate. This has the advantage that poor particle-size estimates are less radiatively influential, because only the associated phase function and single-scattering albedo estimates are affected.

a. Doppler radar method

A radar-based cloud retrieval technique developed for all-ice clouds is presented in Matrosov et al. (2002, 2003). These studies suggest the retrieval can be extended to retrieve the ice component within mixed-phase conditions, using the assumption that the radar is predominantly sensitive to the larger ice particles.

The uncertainties contributing to the IWC and β_i retrievals include the appropriateness to this case study of the individual ice particle bulk density–size relationship for particle sizes $D > 0.1$ mm (Brown and Francis 1995; Locatelli and Hobbs 1974):

$$\rho \approx 0.07 D^{-1.1}, \quad (7)$$

where ρ is given in g cm^{-3} and D in mm, and additionally for the β_i estimate, the mass–area–size relationship, in cgs units,

$$\frac{m}{A_p} = 0.038 D^{0.576} \quad (8)$$

[A. Heymsfield 2003, personal communication; Heymsfield et al. (2002)], where m is the individual particle mass.

Another assumption is that of an exponential ice particle size distribution. This assumption may underestimate the small particle population (e.g., Ivanova et al. 2001). For all-ice Arctic clouds, particles less than 50 μm contribute approximately 20% to the IWC and 40% to the area and hence extinction (Boudala et al. 2002). It is possible that in mixed-phase conditions, fewer small ice particles exist and the exponential distribution assumption is more applicable.

A comparison of cloud optical thicknesses retrieved from radar and infrared radiometer measurements for all-ice SHEBA clouds with infrared absorption optical depths less than 3, indicate an underestimate of 14% in the mean radar-derived cloud optical depth, with a standard deviation of approximately 80% (Matrosov et al. 2003). Individual point aircraft–radar comparisons for a different cloud type are inherently more uncertain. Regardless, the radar retrieval of IWC is expected to be more robust than that of β_i because it depends on fewer assumptions. Overall, retrieval accuracies for IWC, β_i, and $D_{e,i}$, are conservatively estimated by about a factor of 2.

b. Radar–aircraft comparison

A feature of the CPI data is that the individual particle area and perimeter are known. This information, in addition to particle length and width, improves estimates of IWC (Baker et al. 2002; Boudala et al. 2002). A reflectivity and IWC calculation that assumes the Brown and Francis (1995) density–size relationship is also done to facilitate a direct comparison to the retrieval method of Matrosov et al. (2002). The FSSP data were left uncorrected for this comparison, so that the values for the liquid component represent an overestimate.

Figure 9 shows comparisons for 4 May between radar-derived and aircraft-derived values for (a) radar reflectivity, (b) extinction coefficient, (c) ice and liquid

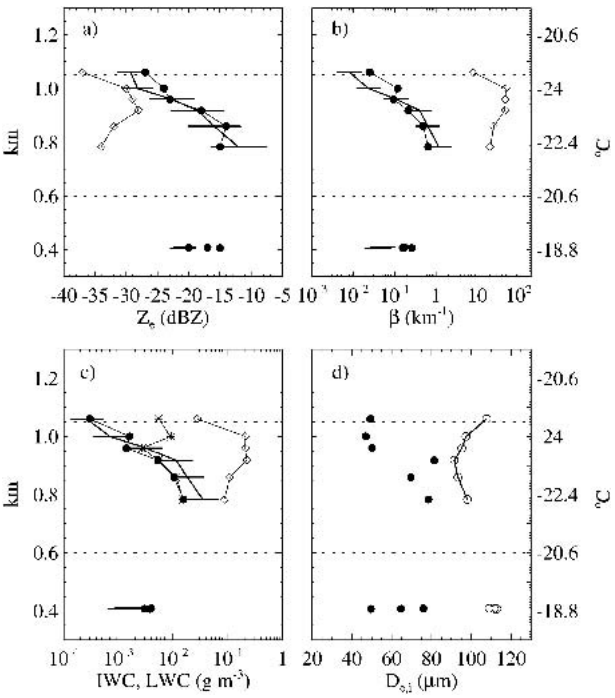

FIG. 9. Comparisons for the 4 May aircraft overflights of the cloud radar between the radar-derived ice microphysics (black line with error bars) and aircraft-derived microphysical values for liquid and ice (diamonds and filled circles) of (a) reflectivity, (b) volume extinction coefficient, (c) liquid and ice water content, and (d) effective ice particle diameter (open circles denote the radar values). Two different methods for calculating IWCs from the aircraft data are shown: the asterisks assume the Brown and Francis (1995) particle density–size relationship, while the filled circles follow the Baker et al. (2002) method. Dotted lines indicate the liquid cloud boundaries.

water content, and (d) effective ice particle diameter. The aircraft data come from the horizontal overpasses depicted in Fig. 3 and described in section 2c. The comparisons within the mixed-phase region are more robust lower in the cloud where the ice concentrations were higher. In contrast to the homogeneity of the liquid water field, the ice hydrometeor field can be highly variable, as indicated by the standard deviations of the cloud radar reflectivity values about a 20-min mean (Fig. 9a). The mean aircraft and radar ice reflectivity values are similar, confirming that the liquid component contributed negligibly to the radar reflectivity (and independently confirmed by low reflectivities calculated from the FSSP data alone).

Figure 9c shows that the radar-retrieved IWCs are slightly higher than the aircraft values, but they agree to within the uncertainty of the comparison (~ factor of 2). At the upper part of the cloud, much of the contribution to the IWC comes from unrimed, large, complex particle shapes, reflecting sedimentation from upper ice clouds. For these large particle sizes, the Baker et al. (2002) method appears to agree better with the radar-retrieved IWC values than the method using the Brown and Francis (1995) density–size relationship. The aircraft overestimate of the low reflectivity values shown in Fig. 9a may support this, as it is similarly computed assuming the Brown–Francis density relationship.

The radar retrievals of β_i are also usually slightly higher than the aircraft values. The worst comparison, as expected, occurs between the radar-retrieved and aircraft $D_{e,i}$. The radar $D_{e,i}$ exceed the aircraft $D_{e,i}$ by factors between 1 and 2. Since $D_{e,i}$ is derived from the ratio of IWC to β_i, this means the radar IWC estimate exceeds the aircraft IWC estimate proportionally more than the radar β_i estimate exceeds the aircraft β_i. Since the radar IWC estimate is not as sensitive to the small particle population and does not use a particle mass–area–size assumption [Eq. (8)], this again suggests that the density–size relationship [Eq. (7)] is primarily responsible for the radar $D_{e,i}$ overestimate (if the aircraft measurements are valid). The aircraft and radar retrievals of $D_{e,i}$ diverge farther from each other in the upper part of the cloud. The radar retrieval of β_i and therefore $D_{e,i}$ is less certain here, as the assumed ice particle mass–area–size relationship Eq. (8) may not apply well to this region containing uniquely large, irregular ice particle shapes.

It is of further interest that the effective particle diameter measured by the aircraft spans values between 50 and 80 μm. An empirical particle size dependence on temperature and IWC has been developed by Boudala et al. (2002) for all-ice high-latitude clouds using aircraft data; their work predicts a $D_{e,i}$ of approximately 40 μm for a temperature of -20°C and IWC of 10^{-2} g m^{-3}. The larger particle sizes shown in Fig. 9d are thought to reflect the more rapid growth of ice particles occurring within a mixed-phase environment that is 20% supersaturated with respect to ice, than will occur in all-ice conditions.

In summary, two robust conclusions relevant to this study can be made from Fig. 9. One is that the total cloud optical depth is dominated by the liquid component (Fig. 9b). The second is that the radar retrievals of β_i and IWC (Figs. 9b, c) agree with the aircraft-determined values to within the retrieval uncertainty, even at liquid and ice water contents of 0.2 and 0.001 g m^{-3}, respectively.

c. *The 1–10 May ice phase time series*

The time series of the radar-retrieved ice β_i and effective radius (= 0.5 $D_{e,i}$), and total ice optical depth and layer-averaged ice particle radius are shown in Fig. 10. The effective radius is shown rather than the effective diameter to aid comparison to Fig. 8. The mean ice cloud optical depth is 0.24, with occasional values of 2 to 6. The layer-mean effective radius is 49 $\pm$7 μm, close to the mean IWC-weighted effective radius of 46, and varies little. Increased values for β_i are evident within the lower cloud at times when upper clouds are present.

d. *Radiative impact of the ice*

Two mechanisms by which ice can diminish LWP and thereby the cloud optical depth are evident in Fig. 11,

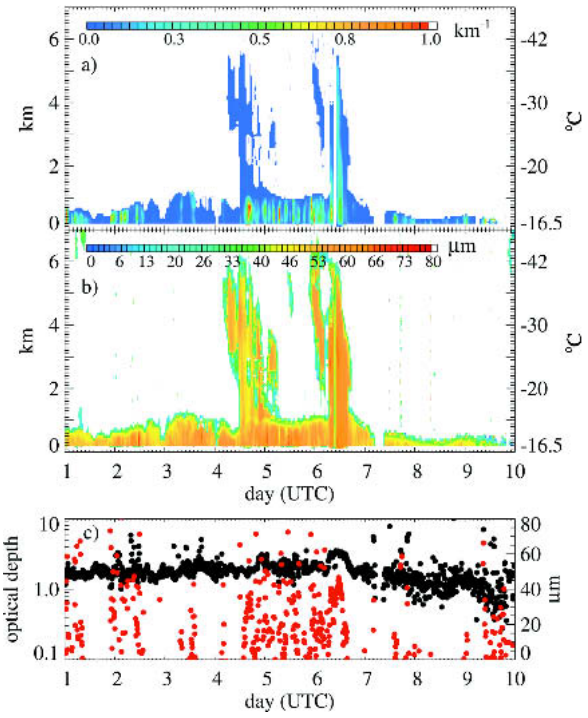

FIG. 10. Radar-retrieved ice (a) volume extinction coefficients, (b) effective ice particle radius, and (c) total ice cloud optical depth (red) and mean effective ice particle radius (black), from 1 to 10 May. Mean temperature sounding values are indicated on the right y axis.

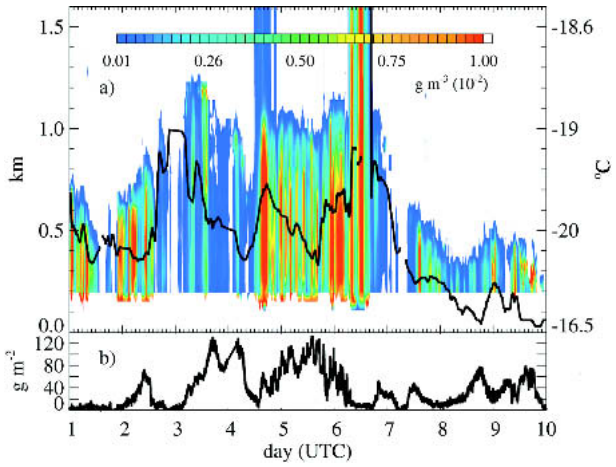

FIG. 11. (a) Radar-retrieved ice water contents from 1 to 10 May, with the lidar-determined liquid cloud base (black line), and (b) MWR-determined LWPs. Mean temperature sounding values are shown on the right *y* axis.

which shows a time series of the IWCs and LWPs. The first is upper ice cloud sedimentation into the lower liquid-bearing cloud on 4 and 6 May. This is associated with a near-complete and complete depletion of the LWP.[6] The second mechanism, apparent on 5 May in particular, is a local variability in IWC associated with smaller changes in LWP, occurring on a time scale of a few hours.

The mechanism for the locally produced IWC has been suggested by MCSZ and involves a cycle wherein liquid droplets above a diameter threshold of approximately 20 μm freeze preferentially, grow, acrete, and fall out (Hobbs and Rangno 1985; Korolev et al. 2003; Rangno and Hobbs 2001). Thereafter, new ice particles are not produced again until coalescence–collision builds up a population of large drops. Only a small population of large drops exceeding a threshold diameter are necessary (Hobbs and Rangno 1985); the existence of large drops in our case, despite the high cloud droplet concentrations and narrow droplet distribution width, is supported by the values shown in Fig. 8. For example, on 5 May, cloud-top effective diameters of over 16 μm are retrieved. Drizzle droplets were also observed by the 4 May aircraft research flight after 2300 UTC (Lawson et al. 2001).

5. Synoptic influence on cloud optical depth

Large-scale synoptic conditions influenced the cloud optical depth in several ways. Variatons in the liquid cloud optical depth are synchronized with boundary layer depth changes (Fig. 8) that attest not only to strong water vapor fluxes (local or large-scale advection), but also to variability in the large-scale subsidence. Figure 12c shows the National Centers for Environmental Predictions (NCEP) reanalysis daily-mean 850-hPa vertical velocities near the SHEBA site; positive values indicate subsiding motion. Surface pressure maps provide context. During 1–3 May, a low pressure region existed to the northwest of the SHEBA site (Fig. 12a), with the site's surface pressure further reduced on 3 May by a front moving from the continent to the north. Thereafter, a broad high pressure region established itself southwest of the SHEBA site and moved to the northeast from 7 to 9 May (Fig. 12b; see also Wylie and Hudson 2002).

Days with rising motion indicated in the 850-hPa vertical velocities coincide with the most optically thick clouds (3 and 5 May). Upper-level ice clouds brought in by southerly winds also appeared on 4 and 6 May, following the frontal passage on 3 May. After 7 May, the thinning low cloud coincided with increased subsidence.

Interestingly, changes in the local ice production activity also appear influenced by the large-scale synoptics. The mechanism should be—and is often observed to be—more active during times when the boundary layer is deeper and the LWPs are higher, creating more opportunities for the formation of large liquid cloud drops (e.g., 5 May; Fig. 11).

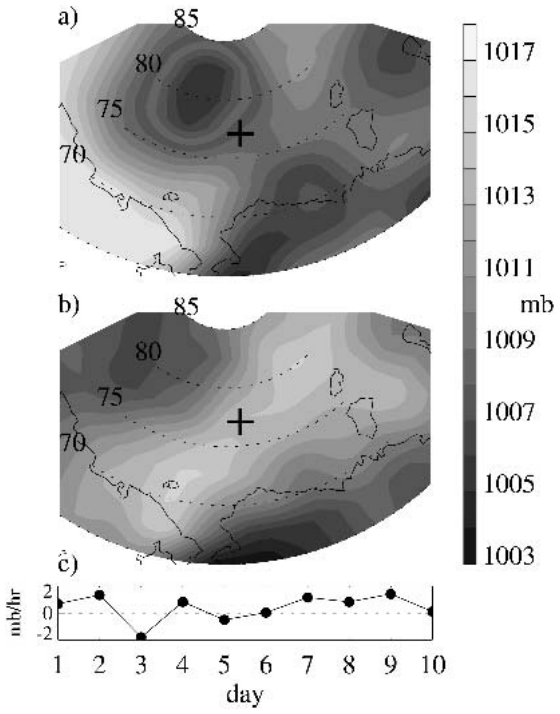

FIG. 12. Mean sea level pressure from (a) 1–3 May, and (b) 4–9 May, and (c) daily-mean 850-hPa vertical velocity at 75°N, 165°W, with positive values indicating subsidence. The location of the SHEBA ice camp is indicated by a plus sign in (a) and (b).

[6] These upper clouds are not included in the model simulation of Carrió et al. (2005).

A counterexample that may be linked to varying entrainment of the aerosol within the overlying air is also evident. Little ice production occurs in the latter half of 3 May and the beginning of 4 May, despite a relatively deep boundary layer, high LWPs, and cloud-top effective radii similar to that of 5 May (Fig. 11). The contact nucleation mechanism of Hobbs and Rangno (1985) proposes that particular aerosol particle types ("contact nuclei") come into contact with supercooled liquid drops and cause them to freeze at a higher temperature than they would through other modes of nucleation. The NCEP 850-hPa vertical velocity on 3 May is more strongly upward than on 5 May, implying a weaker cloud-top entrainment on 3 May, given the similar cloud-top heights for the two days. The diminished availability of contact nuclei may explain the smaller IWCs retrieved for 3 May.

6. Sensitivity analysis for the liquid volume extinction coefficient

The much larger liquid cloud optical depth means that the radiative (flux) impact of the cloud is close to that of a pure liquid cloud. We rely strongly on the adiabatic assumption for the liquid's characterization. This is because cloud radar measurements applied within all-liquid cloud conditions to derive liquid cloud microphysical values (Frisch et al. 1995, 1998, 2002; Shupe et al. 2001) and the liquid volume extinction coefficient (Zuidema and Evans 1998), cannot be used in mixed-phase (or light drizzle) conditions. A sensitivity analysis demonstrates that an adiabatic characterization of β is also more robust than a cloud radar-based estimate lacking additional information on N, as the adiabatic calculation is less sensitive to variability in N and $\sigma_{\log}$.

The extinction can be expressed in terms of LWC, N, and $\sigma_{\log}$ as

$$\beta = 1.65(\pi N)^{1/3}\left(\frac{\mathrm{LWC}}{\rho_w}\right)^{2/3}\exp(-\sigma_{\log}^2), \tag{9}$$

by combining Eq. (5) with Eq. (4). The sensitivity of β to N, $\sigma_{\log}$, and LWC is

$$\frac{\partial \ln\beta}{\partial \ln N} = \frac{1}{3}, \tag{10}$$

$$\frac{\partial \ln\beta}{\partial \ln\sigma_{\log}} = -2\sigma_{\log}^2, \tag{11}$$

$$\frac{\partial \ln\beta}{\partial \ln\mathrm{LWC}} = \frac{2}{3}. \tag{12}$$

For a retrieval of β based upon cloud radar data and an assumed number concentration,

$$\beta = \frac{\pi}{2}\exp(-4\sigma_{\log}^2)Z^{1/3}N^{2/3} \tag{13}$$

(Frisch et al. 1995). Excluding the radar reflectivity, the sensitivity of β is only on N and $\sigma_{\log}$:

$$\frac{\partial \ln\beta}{\partial \ln N} = \frac{2}{3}, \tag{14}$$

$$\frac{\partial \ln\beta}{\partial \ln\sigma_{\log}} = -8\sigma_{\log}^2. \tag{15}$$

The latter cloud-radar-based derivation of β is 4 times more sensitive to variations in $\sigma_{\log}$ and twice as sensitive to variations in N than an adiabatic characterization.

Equations (10)–(15) assume that N is not known. If a microwave radiometer is available along with the cloud radar, a number concentration can be derived and implemented within the cloud radar retrieval. In that case, the sensitivities of the cloud radar/radiometer technique are similar to those for the adiabatic characterization. Both approaches will have a similar sensitivity to the LWC uncertainty, although the source of the uncertainty will be different (MWR versus some assumed fraction of the adiabatic maximum). For the low LWP cases common to the Arctic, a purely adiabatic characterization is also sensitive to how well the cloud boundaries are known (as demonstrated for 7 May in Fig. 7).

7. Radiative flux closure and cloud forcing

A comparison of the observed and modeled radiative fluxes at the surface over the 1–8 May time period further encourages confidence in the data and the retrievals. The calculated net cloud forcing demonstrates that the clouds provided a net warming of the surface compared to clear-sky conditions with the same temperature and humidity structure. Sensitivity tests elucidate the radiative impact of uncertainty in the LWPs and surface reflectances, as well as their importance within climate change scenarios.

a. Data and method

Radiative fluxes were calculated with the medium-band (24 shortwave and 105 longwave bands, the latter at 20 cm^{-1} resolution) radiative transfer model Streamer (Key 2001). The cloud radiation uses a discrete ordinates code (DISORT version 2; Stamnes et al. 2000) with 48 streams. A strength of the model is its comprehensiveness and adaptability for the Arctic climate. For example, the model allows for the representation of two separate phases within a single volume, and shortwave ice cloud optical property parameterizations for seven different ice particle habits are available (Key et al. 2002). An Arctic haze aerosol profile is also available as one of the standard model choices. The model shortwave spectral resolution should adequately represent the observed spectral variation of surface albedo. A model weakness with impact for the radiative flux comparison is that only four gases are considered (H_2O, O_3, CO_2, and O_2) and the gaseous line informa-

tion database is outdated (LOWTRAN 3B, Selby et al. 1976). We modified Streamer to incorporate Mie phase functions (for the liquid phase) and the radar data.

Objective examination of the CPI imagery determined that on 4 and 7 May, most of the contribution to the total ice mass and area came from irregular aggregates, including some rimed aggregates and complex single crystals classified as aggregates. The dominance of the aggregate shape is consistent with a more comprehensive analysis of Arctic ice cloud properties (Korolev et al. 1999).

SHEBA spectral surface albedo data (Perovich et al. 2002) were averaged and extrapolated to match the Streamer spectral resolution, and interpolated in time to a daily resolution. A time-mean broadband albedo of 0.86 typified the dry-snow-covered icescape, with a standard deviation of almost zero. This mean broadband albedo matches the mean albedo calculated from the surface radiation fluxes measured at the Atmospheric Surface Flux Group (ASFG) tower. The ASFG albedos are more variable, with a standard deviation of 0.05. The observed fluxes have a downwelling shortwave flux uncertainty of ±3% with a bias of −5 to +1 W m^{-2}, and a downwelling longwave flux uncertainty of ±2.5 W m^{-2} (Persson et al. 2002).

The Arctic haze aerosol vertical profile was constrained using total aerosol optical depth data derived from sunphotometer measurements (R. Stone 2003, personal communication). In late April the total aerosol optical depth increased sharply, and thereafter slowly diminished with time. Clear-sky measurements made on 25 April (all day) and 7 May (0530–0830 UTC) correspond to total aerosol optical depths interpolated to 0.6 μm of 0.144 and 0.124, respectively, using an Ångström exponent derived from the optical depths at 0.5 and 0.675 μm. Column ozone amounts from the Total Ozone Mapping Spectrometer were used to scale the McClatchey Arctic vertical ozone profile; 393 Dobson units were measured on 18 and 24 May (J. Pinto 2003, personal communication).

Initially, clear-sky conditions were modeled to evaluate the aerosol specification. Hourly averaged 7 May modeled and observed shortwave and infrared fluxes agree to within 1 W m^{-2}. Also, 7 May was modeled using the higher aerosol optical depth value from 25 April, which decreased the modeled surface shortwave radiative fluxes by 2 W m^{-2}. On the basis of these comparisons, a time-mean aerosol optical depth of 0.135 (at 0.6 μm) was used for the 1–10 May time period. Deviations from this value not exceeding the sun photometer observations for 25 April and 7 May can only account for a variation of 2 W m^{-2} in the downward shortwave flux.

b. Comparison

The comparison between the modeled and observed broadband downwelling infrared and shortwave surface fluxes is shown in Fig. 13. The infrared flux comparison

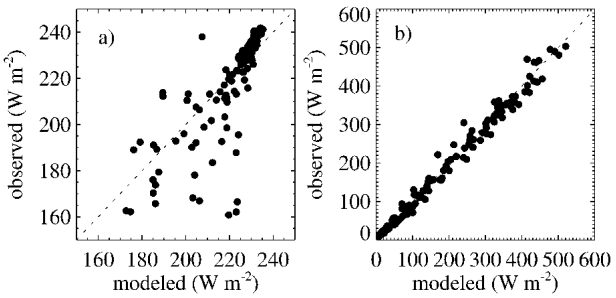

FIG. 13. Modeled and observed broadband downwelling surface (a) infrared fluxes and (b) shortwave fluxes from 1 to 7 May (8 and 9 May were excluded because the observed fluxes were suspect, containing a diurnal cycle offset of approximately 1 h from the modeled fluxes). Only cloudy values are shown.

appears worse than the solar flux comparison, but only because a much smaller range of values is plotted. Over 1–8 May the modeled downwelling surface longwave fluxes exceed the observed surface longwave fluxes by 1 W m^{-2}, with a root-mean-square (rms) deviation of 13 W m^{-2}, or 7% of the observed values. The modeled downwelling surface shortwave fluxes exceed the observed fluxes by 3 W m^{-2} (1% of the observed fluxes), with an rms deviation of 17 W m^{-2}, or 12% of observed fluxes. The small bias encourages confidence in the data, although complete agreement cannot be achieved without exceeding estimated uncertainties in LWP and the surface reflectance (see section 7d). The bias is slightly larger for low LWP time periods (2 and 3.5 W m^{-2} for the longwave and shortwave comparisons, respectively). This indicates the value of incorporating the MWR-derived LWPs, but the small bias again suggests that the cloud was close to its adiabatic maximum throughout this time period.

c. Cloud forcing

By early May, the sun was at or above the horizon, with a mean and noontime solar zenith angle of approximately 74° and 60°, respectively. The all-sky downwelling shortwave fluxes were decreased significantly by the persistent cloud presence, a time-mean decrease of 55 W m^{-2} relative to clear-sky conditions. This exceeded the increase in downwelling longwave fluxes of 49 W m^{-2} compared to clear skies. Nevertheless, because of the high surface albedo, the shortwave cloud forcing[7] averaged only −12 W m^{-2}, whereas the time-mean longwave cloud forcing was 53 W m^{-2}. The time-mean net cloud forcing of 41 W m^{-2} was modu-

[7] The net cloud forcing is the sum of the longwave and shortwave cloud forcing, where each separate cloud forcing is the difference between the net surface flux with the cloud, and without the cloud (as calculated from Streamer). The net surface flux is the difference between the downwelling and upwelling fluxes, where both are positive quantities. A positive cloud forcing represents a warming of the surface.

lated by a diurnal amplitude of approximately 20 W m^{-2}. For the sake of comparison, 40 W m^{-2} is capable of warming 1 m of ice by 1.8 K day^{-1}, neglecting heat transport. For some days (2, 7, and 9 May) a diurnal cycle in the cloud optical depth was observed, which is also typical for lower-latitude stratus, with a nighttime maximum and cloud thinning during and after solar noon (Wood et al. 2002; Zuidema and Hartmann 1995). Such a cloud diurnal cycle further minimizes the diurnal-mean surface shortwave cloud forcing.

At the top of the atmosphere, the net cloud forcing is small and positive (1.4 W m^{-2}); the clouds are slightly more reflective and cooler than the surface. This also implies that the cloud has little impact on the atmospheric radiative structure above the boundary layer.

The net cloud surface forcing is shown as a function of cloud optical depth in Fig. 14. Approximately 30% of the cloud optical depths were less than 3, and almost 60% were greater than 6. For cloud optical depths less than 3, the net cloud forcing is dominated by the longwave component, and is highly sensitive to optical depth. For cloud optical depths greater than 6, the longwave cloud forcing is relatively independent of cloud optical depth, and instead, the net cloud forcing is modulated by the shortwave component. This modulation is at best one-half of the mean net cloud forcing, varying mostly with solar zenith angle and cloud optical depth, given the near-constant surface reflectance. Changes in the surface reflectance will alter the envelope of this modulation.

d. Sensitivity of cloud forcing to surface reflectance and LWP

We analyze the sensitivity of the cloud forcing to those input variables that are both uncertain and important to the radiative forcing. The implications for future climate change scenarios are discussed in section 9. A satellite-based study of Antarctic cloud radiative forcing concludes that cloud forcing is most sensitive to changes in cloud amount, surface reflectance, cloud optical depth, and cloud-top pressure (Pavolonis and Key 2003). For the case examined here, cloud amount is almost constantly high and the cloud-top pressure is well-determined by the 4 times daily soundings. We focus on the LWP values, which have uncertainties of ± 10 g m^{-2}, and on potential surface reflectance uncertainties.

All MWR-derived LWPs were altered by ± 5 and ± 20 g m^{-2}, serving as an upper bound on the impact of random uncertainty and uncertain biases from, for example, over- or underestimated cloud liquid absorption values for the below-freezing conditions. All adiabatically calculated LWPs were corrected to the MWR-derived LWP (i.e., no threshold was considered). Changes in the longwave and shortwave cloud forcing compensated each other for much of the LWP change. An increase in the LWP of 5 and 20 g m^{-2} led to an increased net cloud forcing of 2 and 3 W m^{-2}. The small sensitivity occurs because most cloudy columns are already optically thick, so that the radiative impact is insensitive to further increases. A decrease in the LWP of 5 and 20 g m^{-2} leads to a decrease in the net cloud forcing of -3.5 and -10 W m^{-2}, respectively. This sensitivity is stronger because more cloudy columns become optically thin.

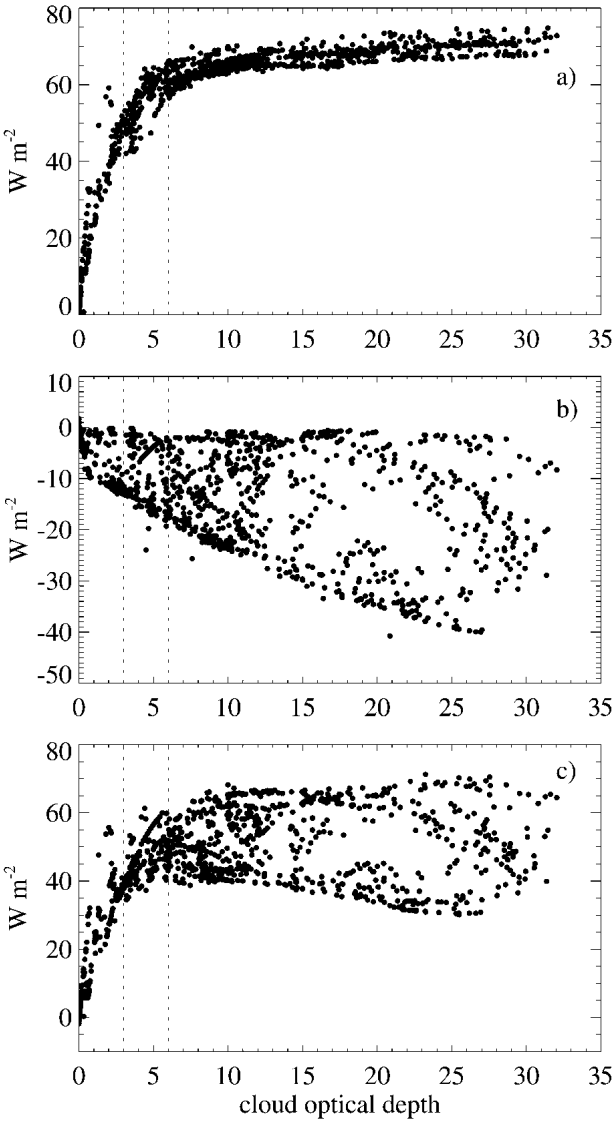

FIG. 14. (a) Longwave, (b) shortwave, and (c) net cloud surface forcing as a function of cloud optical depth. Dotted lines denote optical depths of 3 and 6.

Uncertainties in the surface reflectance arise from spatial and temporal sampling limitations, and natural variability arising from overhead cloudiness preferentially absorbing certain wavelengths, and solar zenith angle changes. A change in the surface reflectance of -0.05 and $+0.05$ changes both the mean shortwave and net cloud forcing by -3.8 and $+4.5$ W m^{-2}, respectively.

8. Impact of radiation on the cloud life cycle

Ignoring the interruptions introduced by the upper-level clouds, the long-lived colloidal stability of this case contrasts with a previous modeling study that finds quick depletion of liquid with ice nuclei concentrations of 4 L^{-1} and a cloud top of $-13°C$ (Harrington et al. 1999). This study's case experiences not only higher supersaturations with respect to ice than calculated within the Harrington et al. (1999) modeling study, but also a higher mean observed ice nuclei concentration of 18 L^{-1}, with maxima of 73 L^{-1} on 4 May and even 1645 L^{-1} on 7 May (see Table 2; Rogers et al. 2001).

The observed longevity may attest to strong water vapor fluxes (either local or large-scale advection) but is surely encouraged at times by strong cloud-top radiative cooling rates. From 4 to 6 May, cloud-top cooling rates exceeded 65 K day^{-1} (not shown). As discussed in Pinto (1998), at cooling rates exceeding 50 K day^{-1}, cloud lifetimes will exceed a day regardless of the ice nuclei concentrations. The higher fall speeds associated with this case's rimed aggregates (rather than more pristine cloud shapes) also aid the cloud longevity (e.g., Harrington et al. 1999).

The high radiative cooling rates generate enough turbulence to promote mixing down to the surface, facilitating surface sensible and latent heat fluxes that help maintain the cloud layer (Wang et al. 2001). This helps explain the observation of Curry et al. (2000) that surface-based mixed layers are thought uncommon in the Arctic, but that their occurrence is most likely in May when the surface is warming rapidly.

On 7 May and thereafter, 850-hPa subsidence rates increased (Fig. 12), and are associated with cloud thinning. The accompanying cloud-top cooling rates diminished to 35 K day^{-1}, their weakness providing a feedback facilitating the mixed-phase cloud dissipation. A diurnal cycle in the cloud-top cooling is more evident after 7 May, with solar warming offsetting the longwave cooling near solar noon (approximately 2300–2400 UTC), further aiding dissipation (not shown).

9. Summary and discussion

Arctic mixed-phase clouds are common, challenging to characterize, important to the Arctic surface energy budget, and poorly represented in large-scale models. Surface-based remote sensors can characterize clouds with greater confidence than is practical with current satellite instruments, and provide a larger-scale context to aircraft data analyses. In the study presented here, we have undertaken an analysis of a mixed-phase cloud with a temperature of approximately $-20°C$ existing from 1 to 10 May at the SHEBA site. The cloud resides within a surface-based mixed layer, and upper ice clouds were present on two of the days, with the 4 May upper cloud so thin it was not detected by human observers.

The liquid cloud base is identified through a low lidar depolarization ratio, a temperature inversion indicates the cloud top, and the MWR-derived LWP constrains an adiabatic parcel calculation of the liquid water content. The MWR uses improved absorption models from those of the initial SHEBA retrievals (Dong et al. 2001; Westwater et al. 2001). The physical retrieval additionally incorporates the liquid cloud temperature, reducing the retrieved LWP uncertainty to 10 g m^{-2}. This is a valuable improvement over the statistical retrieval error of 25 g m^{-2} for the typically low-liquid-water Arctic clouds. An adiabatic characterization, when applicable, is particularly useful for mixed-phase or (lightly) drizzling situations where cloud radar measurements cannot identify the cloud liquid component.

Aircraft observations from two vertical profiles on 4 May and three profiles on 7 May establish the liquid cloud droplet number concentrations and droplet distribution widths, for an $\overline{N}$ of 222 cm^{-3} and $\overline{\sigma_{\log}}$ of 0.242. A homogeneity was observed within the liquid water field, with similar values for N and $\sigma_{\log}$ on 4 and 7 May, and little horizontal-scale LWC variability for 4 May. A sensitivity analysis demonstrates that a volume extinction coefficient constructed from the adiabatically derived LWC, N, and $\sigma_{\log}$ is less sensitive to variability and uncertainty in those three variables than a β derived from cloud radar data, in all-liquid situations where both techniques can be applied and no MWR measurements are available.

Ice microphysical retrievals are done using 35-GHz cloud radar measurements. In contrast to the liquid water field, the ice hydrometeor field is highly inhomogeneous. Despite the presence of much greater LWCs than ice water contents (0.2 and 0.001 g m^{-3}, respectively), the ice component is responsible for almost all of the (radar) reflectivity. This supports the suggestion of Matrosov et al. (2002, 2003) that radar-only retrievals originally designed for all-ice clouds can be extended to mixed-phase conditions. The radar and aircraft estimates of IWC and volume extinction coefficient agree to within the radar retrieval uncertainty (estimated as a factor of 2). The radar retrievals accurately capture the vertical variation in IWC and β_i. Calculations of the IWC using the method of Baker et al. (2002) may perform better (judged by the comparison to the radar retrievals at low IWC values) than IWCs calculated using the Brown and Francis (1995) density relationship.

The effective particle diameter is determined from the ratio of the estimated IWC to β_i; the independent estimate of β_i means that uncertainty in the effective particle diameter estimate only impacts the single-scattering albedo and phase function or asymmetry parameter. The radar-estimated $D_{e,i}$ exceed the aircraft values by factors between 1 and 2. If the aircraft measurements are valid, the Brown–Francis density relationship may be primarily responsible for the radar overestimate. The aircraft effective particle diameter is

large relative to that measured in all-ice clouds (Boudala et al. 2002), and may reflect more rapid growth within the enhanced supersaturated environment (with respect to ice) of the mixed-phase cloud.

Over the 9-day time span, the mean liquid optical depth is approximately 10 with maxima of 30, and the mean ice cloud optical depth is 0.2 with maxima of 2 to 6. The much greater liquid cloud optical depth means that the radiative (flux) impact of the cloud is close to that of a pure liquid cloud. A radiative flux closure calculation finds good agreement between surface observed and calculated fluxes, with the downwelling surface broadband infrared and solar fluxes agreeing to within 1 and 3 W m^{-2}, respectively, over 1–8 May. Both biases are within 1% of the observed fluxes.

Previous studies have highlighted the sensitivity of mixed-phase cloud longevity to modest ice freezing nuclei concentrations (Harrington et al. 1999; Jiang et al. 2000; Pinto 1998). In the study presented here, two mechanisms were observed by which ice affected the cloud LWC and optical depth. One mechanism is the sedimentation of ice particles from an upper cloud on 4 and 6 May, leading to near depletion of the liquid and large decreases in cloud optical depth. The other is a local ice production mechanism with a time scale of a few hours; it is particularly pronounced for 5 May (Fig. 11). Its impact on the cloud optical depth is less significant, with LWP decreases on the order of 25%. One plausible explanation for the locally generated ice particle population is a preferred freezing of liquid droplets exceeding a diameter threshold of approximately 20 μm (Hobbs and Rangno 1985; MCSZ; Rangno and Hobbs 2001).

Deeper boundary layer depths and higher cloud optical depths coincide with large-scale rising motion at 850 hPa (3 and 5 May; Fig. 12), but the synoptic disturbance is also associated with northwardly advected upper-level ice clouds. Increased subsidence after 6 May coincides with a thinning low cloud. Interestingly, a cloud–aerosol interaction may be apparent in these observations, as the local ice production mechanism appears synoptically influenced, with more activity when the NCEP subsidence rates imply increased entrainment of the overlying polluted air given near-constant cloud-top heights (Fig. 11; contrast 5 and 3 May).

The almost-constant liquid presence attests to strong water vapor fluxes, either through large-scale advection or local processes. Strong cloud-top radiative cooling rates (>50 K day^{-1}) also maintain the mixed-phase cloudy boundary layer despite mean ice nuclei concentrations that are high relative to those examined within modeling studies. These also encourage cloud longevity by promoting mixing down to the surface and facilitating enhanced surface fluxes (Wang et al. 2001).

The radiative impact of the cloud upon the surface is significant: a positive time-mean net cloud forcing of 41 W m^{-2}, modulated by a diurnal amplitude of ~20 W m^{-2}. The consistently positive net cloud forcing is primarily a consequence of the high surface albedo (mean value of 0.86), as downwelling shortwave surface fluxes are decreased more by the presence of the cloud than the downwelling infrared surface fluxes are increased by the cloud presence. Approximately 30% of the cloud optical depths are <3, and almost 60% are >6. For the low-optical-depth cloudy columns, the net cloud forcing is highly sensitive to cloud optical depth. For the high-optical-depth cloudy columns the important sensitivity is to the surface reflectance.

Recent observations indicate an increase in springtime Arctic cloudiness (Stone et al. 2002; Wang and Key 2003) and possibly in cloud optical depth (Dutton et al. 2004). For the case presented here, the cloudiness amount is already high, and a more plausible future climate scenario is an increase in the springtime cloud optical depth. A sensitivity assessment suggests that such an increase may not significantly alter the surface radiation budget at this location (76°N, 165°W), because the majority of the cloudy columns are already optically thick. An increase in the presence of upper-level ice clouds associated with increased synoptic activity, may have a more significant impact on cloud optical depth by discouraging the presence of supercooled liquid.

Acknowledgments. Paquita Zuidema was supported throughout most of this study by a National Research Council Research Associateship Award. The contribution of Robert Stone and Taneil Uttal was supported through the NOAA Studies of Environmental Arctic Change (SEARCH) program. We acknowledge the support of NASA/EOS/Validation Grant S-97895 (Program Manager David O'C Starr) and the NASA/FIRE Arctic Clouds Experiment Grant L64205/14997 towards this research. Jeffrey Key's participation was supported through the NOAA SEARCH program and NSF grant OPP-0240827. Paul Lawson and Brad Baker acknowledge NASA–FIRE–ACE Grant L-14363 and NSF SHEBA OPP-0084314. We thank two anonymous reviewers for their useful comments, in particular the reviewer who drew our attention to comparing this study's aircraft effective ice diameter to that in other studies. Support from NSF SHEBA (Agreements OPP-9701730 and OPP-0084257) for the collection and processing of data from the cloud radar, microwave radiometer, and depolarization lidar is gratefully acknowledged. The NCEP reanalysis data used in Fig. 12 were provided by the NOAA–CIRES Climate Diagnostics Center (available online at http://www.cdc.noaa.gov). Graham Feingold introduced us to the sensitivity analysis notation used in section 6. Streamer is publicly available (http://stratus.ssec.wisc.edu/streamer/).

REFERENCES

Albrecht, B. A., C. Fairall, D. Thomson, A. White, and J. Snider, 1990: Surface-based remote sensing of the observed and the adiabatic liquid water content. *Geophys. Res. Lett.,* **17,** 89–92.

Alvarez, R., W. Eberhard, J. Intrieri, C. Grund, and S. Sandberg, 1998: A depolarization and backscatter lidar for unattended operation in varied meteorological conditions. Preprints, *10th Amer. Meteor. Soc. Symp. on Meteorological Observations and Instrumentation,* Phoenix, AZ, Amer. Meteor. Soc., CD-ROM, 3B. 8.

Baker, B., C. Schmitt, P. Lawson, and D. Mitchell, 2002: Further analysis and improvements of ice crystal mass–size relationships. Preprints, *11th Amer. Meteor. Soc. Conf. on Cloud Physics,* Ogden, UT, Amer. Meteor. Soc., CD-ROM, P2. 15.

Beesley, J. A., and R. E. Moritz, 1999: Toward an explanation of the annual cycle of cloudiness over the Arctic Ocean. *J. Climate,* **12,** 395–415.

Boudala, F., G. Isaac, Q. Fu, and S. Cober, 2002: Parameterization of effective ice particle size for high-latitude clouds. *Int. J. Climatol.,* **22,** 1267–1284.

Brown, P. R. A., and P. N. Francis, 1995: Improved measurements of the ice water content in cirrus using a total-water probe. *J. Atmos. Oceanic Technol.,* **12,** 410–414.

Carrió, G. G., H. Jiang, and W. R. Cotton, 2005: Impact of aerosol intrusions on the Arctic boundary layer and on sea ice melting rates. Part I: 4 May 1998 case. *J. Atmos. Sci.,* in press.

Chapman, W. L., and J. E. Walsh, 1993: Recent variations of sea ice and air temperatures in high latitudes. *Bull. Amer. Meteor. Soc.,* **73,** 33–47.

Chen, Y., J. A. Francis, and J. R. Miller, 2002: Surface temperature of the Arctic: Comparison of TOVS satellite retrievals with surface observations. *J. Climate,* **15,** 3698–3708.

Curry, J. A., 1986: Interactions among turbulence, radiation, and microphysics in Arctic stratus clouds. *J. Atmos. Sci.,* **43,** 90–106.

——, and E. E. Ebert, 1992: Annual cycle of radiative fluxes over the Arctic Ocean: Sensitivity to cloud optical properties. *J. Climate,* **5,** 1267–1280.

——, ——, and G. F. Herman, 1988: Mean and turbulence structure of the summertime Arctic cloudy boundary layer. *Quart. J. Roy. Meteor. Soc.,* **114,** 715–746.

——, W. B. Rossow, D. Randall, and J. L. Schramm, 1996: Overview of Arctic cloud and radiation characteristics. *J. Climate,* **9,** 1731–1764.

——, and Coauthors, 2000: FIRE Arctic Clouds Experiment. *Bull. Amer. Meteor. Soc.,* **81,** 5–29.

Daniel, J. S., S. Solomon, R. Portmann, A. O. Langford, and C. S. Eubank, 2002: Cloud liquid water and ice measurements from spectrally resolved near-infrared observations: A new technique. *J. Geophys. Res.,* **107,** 4599, doi:10.1029/2001JD000688.

Dong, X., G. G. Mace, P. Minnis, and D. F. Young, 2001: Arctic stratus cloud properties and their effect on the surface radiation budget: Selected cases from FIRE ACE. *J. Geophys. Res.,* **106,** 15 297–15 312.

Dutton, E., A. Farhadi, R. Stone, C. Long, and D. Nelson, 2004: Long-term variations in the occurrence and effective solar transmission of clouds as determined from surface-based irradiance observations. *J. Geophys. Res.,* **109,** D03204, doi:10.1029/2003JD003568.

Frisch, A. S., C. W. Fairall, and J. B. Snider, 1995: Measurement of stratus cloud and drizzle parameters in ASTEX with a K_α-band Doppler radar and a microwave radiometer. *J. Atmos. Sci.,* **52,** 2788–2799.

——, G. Feingold, C. W. Fairall, T. Uttal, and J. B. Snider, 1998: On cloud radar and microwave radiometer measurements of stratus cloud liquid water profiles. *J. Geophys. Res.,* **103,** 23 195–23 197.

——, M. Shupe, I. Djalalova, G. Feingold, and M. Poellot, 2002: The retrieval of stratus cloud droplet effective radius with cloud radars. *J. Atmos. Oceanic Technol.,* **19,** 835–842.

Fu, Q., 1996: An accurate parameterization of the solar radiative properties of cirrus clouds for climate models. *J. Climate,* **9,** 2058–2082.

Gerber, H., 1996: Microphysics of marine stratocumulus clouds with two drizzle modes. *J. Atmos. Sci.,* **53,** 1363–1377.

Groves, D. G., and J. A. Francis, 2002: Variability of the Arctic atmospheric moisture budget from TOVS satellite data. *J. Geophys. Res.,* **107,** 4785, doi:10.1029/2002JD002285.

Han, Y., and E. R. Westwater, 1995: Remote sensing of tropospheric water vapor and cloud liquid water by integrated ground-based sensors. *J. Atmos. Oceanic Technol.,* **12,** 1050–1059.

Harrington, J. Y., T. Reisin, W. R. Cotton, and S. M. Kreidenweis, 1999: Cloud resolving simulations of Arctic stratus. Part II: Transition-season clouds. *Atmos. Res.,* **51,** 45–75.

Herman, G. F., and J. A. Curry, 1984: Observational and theoretical studies of solar radiation in Arctic stratus clouds. *J. Climate Appl. Meteor.,* **23,** 5–24.

Heymsfield, A. J., A. Bansemar, S. Lewis, J. Iaquinta, M. Kajikawa, C. Twohy, and M. Poellot, 2002: A general approach for deriving the properties of cirrus and stratiform ice cloud particles. *J. Atmos. Sci.,* **59,** 3–29.

Hobbs, P. V., and A. L. Rangno, 1985: Ice particle concentrations in clouds. *J. Atmos. Sci.,* **42,** 2523–2549.

——, and ——, 1998: Microstructures of low and middle-level clouds over the Beaufort Sea. *Quart. J. Roy. Meteor. Soc.,* **124,** 2035–2071.

Hogan, R., P. Francis, H. Flentje, A. Illingworth, M. Quante, and J. Pelon, 2003: Characteristics of mixed-phase clouds. I: Lidar, radar and aircraft observations from CLARE '98. *Quart. J. Roy. Meteor. Soc.,* **129,** 2089–2116.

Houghton, J. T., L. G. M. Filho, B. A. Callander, N. Harris, A. Kattenberg, and K. Maskell, Eds., 1995: *Climate Change 1995—The Science of Climate Change.* Cambridge University Press, 584 pp.

Intrieri, J., C. Fairall, M. Shupe, P. Persson, E. Andreas, P. Guest, and R. Moritz, 2002a: An annual cycle of Arctic surface cloud forcing at SHEBA. *J. Geophys. Res.,* **107,** 8039, doi:10.1029/2000JC000439.

——, M. Shupe, T. Uttal, and B. McCarty, 2002b: An annual cycle of Arctic cloud characteristics observed by radar and lidar at SHEBA. *J. Geophys. Res.,* **107,** 8030, doi:10.1029/2000JC000423.

Ivanova, D., D. L. Mitchell, W. P. Arnott, and M. Poellot, 2001: A GCM parameterization for bimodal size spectra and ice mass removal rates in mid-latitude cirrus clouds. *Atmos. Res.,* **59–60,** 89–113.

Jayaweera, K., and T. Ohtake, 1973: Concentration of ice crystals in arctic stratus clouds. *J. Res. Atmos.,* **7,** 199–207.

Jiang, H., W. R. Cotton, J. O. Pinto, J. A. Curry, and M. J. Weissbluth, 2000: Cloud resolving simulations of mixed-phase Arctic stratus observed during BASE: Sensitivity to concentration of ice crystals and large-scale heat and moisture advection. *J. Atmos. Sci.,* **57,** 2105–2117.

Key, J., 2001: Streamer user's guide. Cooperative Institute for Meteorological Satellite Studies, University of Wisconsin, 96 pp.

——, P. Yang, B. Baum, and S. Nasiri, 2002: Parameterization of shortwave ice cloud optical properties for various particle habits. *J. Geophys. Res.,* **107,** 4181, doi:10.1029/2001JD000742.

Korolev, A., G. A. Isaac, and J. Hallett, 1999: Ice particle habits in Arctic clouds. *Geophys. Res. Lett.,* **26,** 1299–1302.

——, ——, S. G. Cober, J. W. Strapp, and J. Hallett, 2003: Microphysical characterization of mixed-phase clouds. *Quart. J. Roy. Meteor. Soc.,* **129,** 39–65.

Lawson, R., 2003: Continued quality-control and analysis of aircraft microphysical measurements. Final Report, NASA FIRE.ACE LaRC PO No. L–14,363, 40 pp.

——, B. A. Baker, C. G. Schmitt, and T. L. Jensen, 2001: An overview of microphysical properties of Arctic clouds observed in May and July 1998 during FIRE ACE. *J. Geophys. Res.,* **106,** 14 989–15 014.

Liebe, H. J., G. A. Hufford, and T. Manabe, 1991: A model for the

complex permittivity of water at frequencies below 1 Thz. *Int. J. Infrared Millimeter Waves,* **12,** 659–675.
Locatelli, J. D., and P. V. Hobbs, 1974: Fall speeds and masses of solid precipitation particles. *J. Geophys. Res.,* **79,** 2185–2197.
Matrosov, S., A. V. Korolev, and A. J. Heymsfield, 2002: Profiling cloud ice mass and particle characteristic size from Doppler radar measurements. *J. Atmos. Oceanic Technol.,* **19,** 1003–1018.
——, M. Shupe, A. J. Heymsfield, and P. Zuidema, 2003: Ice cloud optical thickness and extinction estimates from radar measurements. *J. Appl. Meteor.,* **42,** 1584–1597.
Miles, N. L., J. Verlinde, and E. E. Clothiaux, 2000: Cloud droplet size distributions in low-level stratiform clouds. *J. Atmos. Sci.,* **57,** 295–311.
Mitchell, D. L., 2002: Effective diameter in radiation transfer: General definition, applications, and limitations. *J. Atmos. Sci.,* **59,** 2330–2346.
Moran, K. P., B. E. Martner, M. J. Post, R. Kropfli, D. C. Welsh, and K. B. Widener, 1998: An unattended cloud-profiling radar for use in climate research. *Bull. Amer. Meteor. Soc.,* **79,** 443–455.
Morrison, H., J. A. Curry, M. Shupe, and P. Zuidema, 2005: A new double-moment microphysics parameterization for application in cloud and climate models. Part II: Single-column modeling of Arctic clouds. *J. Atmos. Sci.,* in press.
Parkinson, C. L., D. J. Cavalieri, P. Gloersen, H. J. Zwally, and J. C. Comiso, 1999: Arctic sea ice extents, areas, and trends, 1978–1996. *J. Geophys. Res.,* **104,** 20 837–20 856.
Pavolonis, M. J., and J. R. Key, 2003: Antarctic cloud radiative forcing at the surface estimated from the AVHRR Polar Pathfinder and ISCCP D1 datasets, 1985–1993. *J. Appl. Meteor.,* **42,** 827–840.
Perovich, D. K., T. C. Grenfell, B. Light, and P. V. Hobbs, 2002: Seasonal evolution of the albedo of multiyear Arctic sea ice. *J. Geophys. Res.,* **107,** 8044, doi:10.1029/2000JC000438.
Persson, O., C. W. Fairall, E. L. Andreas, P. S. Guest, and D. K. Perovich, 2002: Measurements near the atmospheric surface flux group tower at SHEBA: Near-surface conditions and surface energy budget. *J. Geophys. Res.,* **107,** 8045, doi:10.1029/2000JC000705.
Pinto, J. O., 1998: Autumnal mixed-phase cloudy boundary layers in the Arctic. *J. Atmos. Sci.,* **55,** 2016–2038.
——, J. A. Curry, and J. M. Intrieri, 2001: Cloud–aerosol interactions during autumn over Beaufort Sea. *J. Geophys. Res.,* **106,** 15 077–15 097.
Rangno, A., and P. Hobbs, 2001: Ice particles in stratiform clouds in the Arctic and possible mechanisms for the production of high ice concentrations. *J. Geophys. Res.,* **106,** 15 065–15 075.
Rogers, D. C., P. J. DeMott, and S. M. Kreidenweis, 2001: Airborne measurements of tropospheric ice-nucleating aerosol particles in the Arctic spring. *J. Geophys. Res.,* **106,** 15 053–15 063.
Rosenkranz, P. W., 1998: Water vapor microwave continuum absorption: A comparison of measurements and models. *Radio Sci.,* **33,** 919–928.
Schweiger, A. J., and J. R. Key, 1994: Arctic Ocean radiative fluxes and cloud forcing estimates from the ISCCP C2 cloud dataset. *J. Appl. Meteor.,* **33,** 948–963.
Selby, J., E. Shettle, and R. McClatchey, 1976: Atmospheric transmittance from 0.25 to 28.5 μm. Supplement LOWTRAN 3B. Air Force Geophysics Laboratory, Environmental Research Paper, No. 587, 78 pp.
Serreze, M., and Coauthors, 2000: Observational evidence of recent change in the northern high-latitude environment. *Climatic Change,* **46,** 159–207.
Shupe, M. D., T. Uttal, S. Matrosov, and A. S. Frisch, 2001: Cloud water contents and hydrometeor sizes during the FIRE-Arctic Clouds Experiment. *J. Geophys. Res.,* **106,** 15 015–15 028.
Stamnes, K., S. Tsay, W. Wiscombe, and I. Laszlo, 2000: A general-purpose numerically stable computer code for discrete-ordinate-method radiative transfer in scattering and emitting layered media. DISORT Report Vol. 1.1, 56 pp.
Stankov, B. B., B. E. Martner, and M. K. Politovich, 1995: Moisture profiling of the cloudy winter atmosphere using combined remote sensors. *J. Atmos. Oceanic Technol.,* **12,** 488–510.
Stone, R., 1997: Variatons in western arctic temperatures in response to cloud radiative and synoptic-scale influences. *J. Geophys. Res.,* **102,** 21 769–21 776.
——, J. Key, and E. Dutton, 1993: Properties and decay of stratospheric aerosols in the arctic following the 1991 eruptions of Mount Pinatubo. *Geophys. Res. Lett.,* **20,** 2359–2362.
——, E. Dutton, J. Harris, and D. Longenecker, 2002: Earlier spring snowmelt in northern Alaska as an indicator of climate change. *J. Geophys. Res.,* **107,** 4089, doi:10.1029/2000JD000286.
Sturm, M., C. Racine, and K. Tape, 2001: Increasing shrub abundance in the Arctic. *Nature,* **411,** 546–547.
Sun, Z., and K. Shine, 1994: Studies of the radiative properties of ice and mixed-phase clouds. *Quart. J. Roy. Meteor. Soc.,* **120,** 111–137.
Tao, X., J. E. Walsh, and W. L. Chapman, 1996: An assessment of global climate model simulations of Arctic air temperatures. *J. Climate,* **9,** 1060–1076.
Turner, D., S. Ackerman, B. Baum, H. Revercomb, and P. Yang, 2003: Cloud phase determination using ground-based AERI observations at SHEBA. *J. Appl. Meteor.,* **42,** 701–715.
Uttal, T., and Coauthors, 2002: Surface heat budget of the Arctic Ocean. *Bull. Amer. Meteor. Soc.,* **83,** 255–275.
Vavrus, S., 2004: The impact of cloud feedbacks on Arctic climate under greenhouse forcing. *J. Climate,* **17,** 603–615.
Walsh, J. E., and W. L. Chapman, 1998: Arctic cloud–radiation–temperature associations in observational data and atmospheric reanalyses. *J. Climate,* **11,** 3030–3045.
Wang, S., Q. Wang, R. E. Jordan, and P. O. G. Persson, 2001: Interactions among longwave radiation of clouds, turbulence, and snow surface temperature in the Arctic: A model sensitivity study. *J. Geophys. Res.,* **106,** 15 323–15 333.
Wang, X., and J. R. Key, 2003: Recent trends in Arctic surface, cloud, and radiation properties from space. *Science,* **299,** 1725–1728.
Wang, Z., K. Sassen, D. N. Whiteman, and B. D. Demoz, 2004: Studying altocumulus with ice virga using ground-based active and passive remote sensors. *J. Appl. Meteor.,* **43,** 449–460.
Westwater, E. R., Y. Han, M. D. Shupe, and S. Y. Matrosov, 2001: Analysis of integrated cloud liquid and precipitable water vapor retrievals from microwave radiometers during the Surface Heat Budget of the Arctic Ocean project. *J. Geophys. Res.,* **106,** 32 019–32 030.
Wood, R., C. Bretherton, and D. L. Hartmann, 2002: Diurnal cycle of liquid water path over the subtropical and tropical oceans. *Geophys. Res. Lett.,* **29,** 2092, doi:10.1029/2002GL015371.
Wylie, D., 2001: Arctic weather during FIRE/ACE 1998. *J. Geophys. Res.,* **106,** 15 363–15 375.
——, and J. Hudson, 2002: Effects of long-range transport and clouds on cloud condensation nuclei in the springtime Arctic. *J. Geophys. Res.,* **107,** 4138, doi:10.1029/2001JD000759.
Yum, S. S., and J. G. Hudson, 2001: Vertical distributions of cloud condensation nuclei spectra over the springtime Arctic Ocean. *J. Geophys. Res.,* **106,** 15 045–15 052.
Zhang, T., K. Stamnes, and S. A. Bowling, 1996: Impact of clouds on surface radiative fluxes and snowmelt in the Arctic and subarctic. *J. Climate,* **9,** 2110–2123.
Zuidema, P., and D. Hartmann, 1995: Satellite determination of stratus cloud microphysical properties. *J. Climate,* **8,** 1638–1657.
——, and K. F. Evans, 1998: On the validity of the independent pixel approximation for boundary layer clouds observed during ASTEX. *J. Geophys. Res.,* **103,** 6059–6074.